Isolated Metal Sites in Cu−Zn−Y/Beta for Direct and Selective Butene-Rich C_{3+} Olefin Formation from Ethanol

Junyan Zhang, Evan C. Wegener, Nohor River Samad, James W. Harris, Kinga A. Unocic, Lawrence F. Allard, Stephen Purdy, Shiba Adhikari, Michael J. Cordon, Jeffrey T. Miller, Theodore R. Krause, Sichao Cheng, Dongxia Liu, Meijun Li, Xiao Jiang, Zili Wu, and Zhenglong Li*

Cite This: *ACS Catal.* 2021, 11, 9885−9897 Read Online

ACCESS | Metrics & More | Article Recommendations | Supporting Information

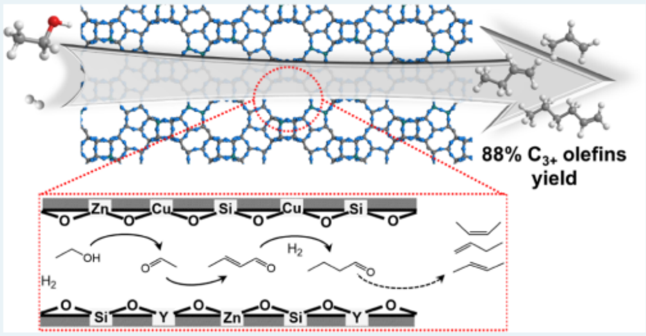

ABSTRACT: Direct and selective production of C_{3+} olefins from bioethanol remains a critical challenge and important for the production of renewable transportation fuels such as aviation biofuels. Here, we report a Cu−Zn−Y/Beta catalyst for selective ethanol conversion to butene-rich C_{3+} olefins (88% selectivity at 100% ethanol conversion, 623 K), where the Cu, Zn, and Y sites are all highly dispersed. The ethanol-to-butene reaction network includes ethanol dehydrogenation, aldol condensation to crotonaldehyde, and hydrogenation to butyraldehyde, followed by further hydrogenation and dehydration reactions to form butenes. Cu sites play a critical role in promoting hydrogenation of the crotonaldehyde C═C bond to form butyraldehyde in the presence of hydrogen, making this a distinctive pathway from crotyl alcohol-based ethanol-to-butadiene reaction. Reaction rate measurements in the presence of ethanol and acetaldehyde (543 K, 12 kPa ethanol, 1.2 kPa acetaldehyde, 101.9 kPa H_2) over monometallic Zn/Beta and Y/Beta catalysts indicate that Y sites have higher C−C coupling rates than over Zn sites (initial C−C coupling rate, 6.1×10^{-3} mol mol_Y^{-1} s^{-1} vs 1.2×10^{-3} mol mol_{Zn}^{-1} s^{-1}). Further, Lewis-acidic Y-site densities over Cu−Zn−Y/Beta with varied Y loadings are linearly correlated with the initial C−C coupling rates, suggesting that Lewis-acidic Y sites are the predominant sites that catalyze C−C coupling in Cu−Zn−Y/Beta catalysts. Control experiments show that the dealuminated Beta support is important to form higher density of Lewis-acidic Y sites in comparison with other supports such as silica, or deboronated MWW despite similar atomic dispersion of Y sites and Y−O coordination numbers over these supports, leading to more than 9 times higher C−C coupling rate per mole Y over dealuminated Beta relative to other supports. This study highlights the significance of unique combination of metal sites in contributing to the selective valorization of ethanol to C_{3+} olefins, motivating for exploring multifunctional zeolite catalysts, where the presence of multiple sites with varying reactivities and functions allows for controlling the predominant molecular fluxes toward the desired products in complex reactions.

KEYWORDS: *ethanol, butenes, olefins, Lewis acid zeolites, single-atom catalysts*

1. INTRODUCTION

Light olefins (C_{3+}) serve as critical building blocks for synthesizing a wide variety of commodity chemicals, polymers, and synthetic hydrocarbon fuels (e.g., gasoline, jet, and diesel).[1−3] These olefins are traditionally produced through either steam cracking or fluid catalytic cracking of naphtha, contributing to over 95%, 89%, and 95% of ethylene, propene, and butene production, respectively.[1,4] The use of shale gas has shifted ethylene production to steam cracking of light paraffins, which primarily generates ethylene with much less C_{3+} olefins,[5,6] so there is a necessity for on-purpose production of C_{3+} olefins. Further, growing concerns about anthropogenic climate change related to CO_2 emissions from petroleum-based operations[7,8] continuously motivate the search for new pathways to produce C_{3+} olefins from renewable resources.[9,10] One such renewable feedstock is ethanol, a key C_2 platform chemical due to its commercial availability (~29 billion gallons globally in 2019[11]) and emerging ethanol synthesis opportunities from lignocellulosic biomass[12] and CO_2.[13] Ethanol conversion to C_{3+} olefins presents great opportunities to produce sustainable middle distillate fuels for decarbonizing the hard-to-electrify sectors, such as aviation, marine, and heavy-duty trucking.[14]

Received: May 13, 2021
Revised: June 28, 2021
Published: July 22, 2021

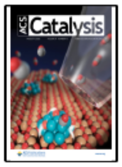

https://doi.org/10.1021/acscatal.1c02177

Ethanol can be converted to C_{3+} olefins through several reaction pathways involving different C−C coupling mechanisms over various acid or base catalysts. One approach involves ethanol dehydration to ethylene and subsequent ethylene oligomerization into butene-rich olefins, which can be accomplished in either one or two process steps.[14] The two-step approach allows for process optimization around each step over separate catalysts[15] (*e.g.*, alumina for ethanol dehydration and nickel/silicoaluminate for ethylene oligomerization); however, the endothermic ethanol dehydration reaction requires significant energy input and the two-step operation leads to increased operating and capital expenses. The single-step approach couples two reaction steps on one single catalyst (generally Brønsted-acidic zeolites[16−18]) and integrates heat generated by the oligomerization step for endothermic ethanol dehydration to reduce both operation and capital costs.[14] This approach, however, catalyzes significant side reactions such as aromatization and hydrogen transfer that lead to considerable aromatic and light paraffin products and decreased C_{3+} olefin yields (<50%).[14]

Alternative ethanol upgrading strategies have been developed utilizing aldol condensation of aldehydes or ketones (*e.g.*, acetaldehyde and acetone) as a primary reaction step. A two-stage reaction pathway can be developed around the Guerbet reaction over basic catalysts (*e.g.*, MgO, hydroxyapatite (HAP)[19]) to convert ethanol into longer-chain alcohols (*e.g.*, 1-butanol), followed by alcohol dehydration to C_{3+} olefins over acid catalysts (*e.g.*, PO_4^{3-} modified γ-Al_2O_3,[20] H-ZSM-5, H-FER, and H-FAU[21]). A major challenge is the limited yield of the targeted alcohols due to competing side reactions that form ketones, aldehydes, dienes, and ethylene when the reaction is performed at high conversion (>50%).[14] Other pathways over metal oxide catalysts[22,23] containing both Lewis acid and basic sites use acetaldehyde or acetone as the intermediate for C−C coupling reactions to form C_4-rich olefin (*i.e.*, isobutene, 1-butene, and 2-butenes) streams. For example, acetaldehyde derived from ethanol dehydrogenation can undergo oxidation and ketonization over $ZnZrO_x$ to form acetone, which dimerizes into C_6 intermediates (*i.e.*, diacetone alcohol or mesityl oxide) and then decomposes to isobutene.[23,24] CO_2 is formed as a major side product during the acetone formation and C_6 intermediate decomposition steps, limiting the maximum isobutene selectivity to 67%.[23,24] Ethanol can also undergo coupling over transition-metal-modified oxide catalysts (*e.g.*, $Ag/ZrO_2/SiO_2$) to form butene-rich olefins under a H_2 environment, where the crotyl alcohol and butadiene were observed as the major intermediates to butenes.[25] A high C_{3+} olefin selectivity can be achieved (∼69% at near complete ethanol conversion, 673 K, 77 kPa ethanol balanced with H_2, 700 kPa total pressure, weight hourly space velocity (WHSV) = 1.4−1.8 h^{-1}), yet significant formation of side products (*e.g.*, ethylene) is observed (∼19% ethylene yield).[25] Increasing C_{3+} olefin selectivity requires additional catalyst development through either improving existing catalyst compositions and surface properties or through new catalytic material design.

Lewis-acid zeolites containing metal centers such as Sc^{3+}, Y^{3+}, Zr^{4+}, Ti^{4+}, and Nb^{5+}[26−30] can provide C−C bond formation sites to convert acetaldehyde to crotonaldehyde while at the same time avoiding major side product formation (*e.g.*, aromatics, paraffins, and CO_2), making such materials as good candidates for further catalyst design in the ethanol to C_{3+} olefin application. Beyond this, searching for Lewis-acid zeolites that have lower ethanol dehydration activity would minimize ethylene production and further benefit the formation of desired C_{3+} olefins. Among various candidates, Y-containing zeolites can potentially suppress the undesired ethanol dehydration because Y^{3+} is considered as a softer Lewis acid (due to the trivalent nature and larger ionic radius) compared with other Lewis acid sites (*e.g.*, Hf, Zr, and Sc) according to the hard and soft acid and base principle.[29,31,32] Y-containing zeolites have been shown to be active catalysts for ethanol conversion to butadiene;[33,34] however, descriptions of the chemical and catalytic nature of the metal sites within these Y-based zeolite catalysts and their associated catalytic functionalities are still limited. More importantly, the use of Lewis-acid zeolites that contain Y for direct and selective ethanol valorization to butene-rich C_{3+} olefins has not been reported, which requires the exploration of unique combination of metal sites and support to selectively catalyze ethanol conversion to butene-rich olefin products.

Here, we report a Y-containing multifunctional catalyst (Cu−Zn−Y/Beta) capable of selectively converting ethanol to butene-rich C_{3+} olefins, where Cu and Zn are selected to catalyze ethanol dehydrogenation to generate acetaldehyde,[35,36] while Lewis-acidic Y sites are targeted as the aldol condensation sites and Cu sites further catalyze the subsequent hydrogenation of crotonaldehyde to butyraldehyde. Cu, Zn, and Y metal centers on trimetallic Cu−Zn−Y/Beta were characterized with high-angle annular dark-field scanning transmission electron microscopy (HAADF-STEM), X-ray absorption spectroscopy (XAS), and pyridine adsorption transmission Fourier transform infrared spectroscopy (FTIR) to probe metal dispersion, oxidation states and coordination, and Lewis and Brønsted acid sites. The primary reaction network of ethanol to butenes was demonstrated through selectivity−conversion plots when directly feeding ethanol and other reaction intermediates (*e.g.*, acetaldehyde, crotonaldehyde, butyraldehyde, and crotyl alcohol). The roles of each metal within the ethanol-to-butene reaction sequence were also probed by comparing the reaction rates among monometallic, bimetallic, and trimetallic catalysts. Trimetallic Cu−Zn−Y over other supports (deboronated MWW and silica) were also studied as controls to understand the impact of supports on the chemical nature of metal sites and their relative catalytic activities in comparison with Cu−Zn−Y/Beta.

2. MATERIALS AND METHODS

2.1. Catalyst Synthesis. Cu−Zn−Y/Beta catalysts were synthesized via solid-state grinding of Cu, Zn, and Y precursors (metal nitrates) into a dealuminated Beta support (named as DeAl-Beta), which was prepared by acid washing as described in Supporting Information Section S.1.1. Copper nitrate trihydrate (Sigma-Aldrich, 98%), zinc nitrate hexahydrate (Sigma-Aldrich, 97%), and yttrium nitrate hexahydrate (Sigma-Aldrich, 97%) were weighed and mixed with DeAl-Beta in the mortar. The collected solids were ground together for 1200 s until the mixed powder was homogeneous light green without any observable blue particles. The resulting solids were heated to 823 K (0.017 K s^{-1}) for 6 h under 10 cm^3 g_{cat}^{-1} s^{-1} air flow (Airgas, 99.99%). Monometallic and bimetallic catalysts (Cu/Beta, Zn/Beta, Y/Beta, Cu−Y/Beta, and Zn−Y/Beta) were synthesized using a similar procedure. Cu−Zn−Y/MWW and Cu−Zn−Y/silica were synthesized using similar solid-state grinding with details described in Supporting Information Sections S.1.2 and S.1.3. The nominal loadings of Cu and Zn were kept constant as 1.0 and 2.0 wt %, respectively, for all the catalysts. Y loadings were varied between 1.0 and 7.0 wt %, so the catalysts were labeled as Cu–Zn-Y_x/Beta below, where the subscript x indicates the nominal Y loading. For all the other trimetallic catalysts on different supports, the nominal Y loadings were kept as 7.0 wt % and the catalysts were named as Cu–Zn–Y_7/MWW and Cu–Zn–Y_7/silica.

2.2. Catalyst Characterization. Powder X-ray diffraction (XRD) patterns were recorded using a PANalytical X-ray diffractometer (40 kV, 44 mA) using a Cu Kα radiation source (λ = 0.1542 nm). Diffraction patterns were collected from 4 to 40° at a scan rate of 0.04° s^{-1} with a step size of 0.025°. Bulk elemental compositions were determined via inductively coupled plasma atomic emission spectroscopy (ICP-AES) by Galbraith Laboratories, Inc. Nitrogen adsorption isotherms (77 K) were measured on a Quantachrome Autosorb iQ. The samples were degassed under vacuum (<0.002 Torr) to 623 K for 6 h before adsorptive analysis. Micropore volumes were determined from the semilog derivative $\delta(V_{ads}/g)/\delta(\log(P/P_0)$ versus $\log(P/P_0))$ analysis of N_2 adsorption isotherms at the end of micropore filling regimes. STEM and energy-dispersive X-ray spectroscopy (EDS) analyses are reported in Supporting Information Section S.2.

XAS spectra were collected in the transmission mode at the Cu, Zn, and Y K edges on the bending magnet beam line of the Materials Research Collaborative Access Team (MR-CAT) (Advanced Photon Source, Argonne National Laboratory). Energy calibration was performed simultaneously with sample measurements using a third ion chamber on metal foil standards. Detailed procedures for sample preparation, pretreatment, measurement, and analysis are described in Supporting Information Section S.2.

Transmission FTIR analyses were performed using a Nicolet 4700 (Thermo Fisher) spectrometer equipped with a liquid N_2-cooled (77 K) MCT detector. The spectra were collected relative to an empty cell background reference collected under ambient air flow. For each spectrum, 64 scans were averaged at a resolution of 2 cm^{-1} in the range 4000–400 cm^{-1}. Sample pretreatment and measurement procedure are reported in Supporting Information Section S.2.

2.3. Ethanol Conversion. Ethanol conversion was carried out in a tubular quartz reactor (12.7 mm O.D.) with a fixed bed configuration under ambient pressure. The reactor was vertically aligned in a temperature-controlled tubular furnace. The catalyst bed temperature was measured with a K-type thermocouple. Catalysts were pelletized and ground into particle sizes ranging from 125 to 180 μm for low conversion studies, while 90–125 μm particle sizes were used for the high conversion studies. Typically for the high conversion experiments, 0.15 g of each catalyst was pretreated by heating at 0.083 K s^{-1} to 673 K and held at 673 K under He flow (0.33 cm^3 s^{-1}) for 1 h to remove moisture, followed by reduction in 0.33 cm^3 s^{-1} H_2 at 623 K before measurements of catalytic performance. The flow rates of H_2 (Airgas, >99.999%) and He (Airgas, >99.999%) were controlled with mass flow controllers. Pure ethanol (C_2H_5OH, >99%) was fed with a syringe pump (KD Scientific) and vaporized inside the 3.175 mm o.d. stainless steel transfer lines heated to 423 K using electrical heating tapes. The products were analyzed with an online gas chromatograph (Agilent 7820A) equipped with both a flame ionization detector and thermal conductivity detectors. Product identification was performed with a gas chromatograph (Agilent 6850) with a mass spectrometer (Agilent 5975C) and calibrated with known chemical standards. Calculations of ethanol conversion, produce selectivity, and WHSV are described in Supporting Information Section S.3.

The reaction rate measurements were performed in a differential conversion regime (<10% conversion) in the same fixed bed reactor. Typically, 0.01–0.05 g of the catalyst was diluted with 0.8 g of SiC (Alfa Aesar, 120 grit). When acetaldehyde (Sigma-Aldrich, >99.5%) was used as the reactant, it was introduced by flowing H_2 through a bubbler at 245 K and ambient pressure. The carbon balance for high conversion measurements was 92–96%, while it was ~100% for low conversion studies (<10%). Definitions of the corresponding reaction rate are shown in Supporting Information Section S.3. A one-site exponential function was used to fit the transient kinetic profile when feeding acetaldehyde or cofeeding ethanol and acetaldehyde, and the initial C–C coupling rate was calculated by extrapolating to time zero.[37,38] Future studies will probe the causes of deactivation to further refine the model and more precisely represent the origins of the observed deactivation. Nevertheless, the trend in C–C coupling rates would remain similar regardless of the model used.

To obtain the selectivity versus conversion relationship for the reaction network study, conversions of ethanol, acetaldehyde, crotonaldehyde (Sigma-Aldrich, >99%), butyraldehyde (Sigma-Aldrich, >99.5%), crotyl alcohol (Sigma-Aldrich, 96%), and butadiene (Airgas, 3% in N_2) were carried out in the same fixed bed reactor. The WHSV was varied to change the conversions. Catalyst loadings of 0.05 g were used by diluting in 0.8 g of SiC for experiments with ethanol, acetaldehyde, crotonaldehyde, butyraldehyde, and crotyl alcohol in the feed. For butadiene conversion, 0.03 g of the catalyst was used and it was diluted with 0.8 g of SiC. Catalyst pretreatment was the same as in the above high conversion experiments. Acetaldehyde was fed through a bubbler at 245 K at ambient pressure, and hydrogen flow through the bubbler was varied to change the acetaldehyde flow rate. The other liquid reactants (ethanol, crotonaldehyde, butyraldehyde, and crotyl alcohol) were introduced into the reactor using a syringe pump (KD Scientific) with H_2 as the carrier gas.

3. RESULTS AND DISCUSSION

3.1. Catalyst Characterizations. Cu–Zn–Y/Beta, mono-, and bimetallic catalysts were prepared by solid-state grinding of metal precursors into a dealuminated Beta support. ICP-AES measurements indicate that Si/Al ratios increase from 12.5 to ~1300 after dealumination, forming silanol defects (*e.g.*, silanol nests) as a result of removal of Al from the Beta framework[39] and suggesting that no significant Al-derived Brønsted acid sites remain on dealuminated-Beta-supported catalysts. Additional ICP-AES measurements indicate metal loadings of 0.91, 1.7, and 6.6 wt % for Cu, Zn and Y, respectively, on Cu–Zn–Y_7/Beta (Table S1). Monometallic Cu/Beta (1.0 wt % Cu), Zn/Beta (2.0 wt % Zn), and Y/Beta (6.8 wt % Y) catalysts were synthesized as reference materials with XRD patterns (Figure S1) and micropore volumes derived from N_2 adsorption isotherms (77 K), consistent with the Beta topology (Table S2). Additional trimetallic catalysts, with similar metal loadings as Cu–Zn–Y_7/Beta (Table S1), were synthesized on amorphous silica (Cu–Zn–Y_7/silica), and deboronated MWW (DeB-MWW, Cu–Zn–Y_7/MWW), and the corresponding XRD patterns are consistent with the parent siliceous materials (Figure S2). The lack of XRD diffraction

https://doi.org/10.1021/acscatal.1c02177
ACS Catal. 2021, 11, 9885–9897

peaks corresponding to Cu, Zn, or Y metal oxide nanoparticles on all these samples (Figures S1 and S2) suggests the absence of large metal oxide nanoparticle domains on any of the samples included in this study.

HAADF-STEM and EDS were used to probe the distributions of metal species. A standardless quantitative analysis from the spectrum of the large aggregate of Cu–Zn–Y_7/Beta (Figure S3) shows Cu/Zn/Y ratio in this aggregate is in reasonable agreement with the bulk composition of the catalyst measured by ICP-AES (Table S3). Individual elemental maps also indicate each element's overall uniform distribution in the catalyst particles. Similarly, uniform distributions of these metal species are observed on MWW and amorphous silica without obvious metal clusters (Figures S4 and S5), in agreement with the XRD results (Figure S2). High-resolution HAADF-STEM images of Cu–Zn–Y_7/Beta do not show observable metal nanoparticles (>100 areas were measured, representative images shown in Figure S6), suggesting a high dispersion of metal centers on these supports. It is also worth noting that stacked MWW layers are clearly observed in the bright-field-STEM image of Cu–Zn–Y_7/MWW (Figure S7), reflecting the preservation of MWW zeolite textural properties.

Metal oxidation states and the local coordination environment were investigated by *in situ* XAS at the Cu, Zn, and Y K edges. The XAS spectra were collected on the as-synthesized trimetallic samples and after each stage in a series of thermal treatments including oxidation (20 kPa O_2 in 81 kPa He, 823 K), inert treatment (101 kPa He, 673 K), and reduction (3.5 kPa H_2 in 98 kPa He, 673 K). X-ray absorption near-edge spectroscopy (XANES) analysis at the Cu K edge on the as-synthesized Cu–Zn–Y_7/Beta shows a weak absorption peak at 8978.5 eV (Figure 1A), which is caused by the dipole-forbidden 1s → 3d transition of Cu(II),[40,41] indicating the presence of predominantly Cu(II) species in the as-synthesized sample. High-temperature oxidation does not change the Cu oxidation state and yields only a slight decrease in the white line intensity (Figure 1B), potentially reflecting water desorption, which is consistent with the slight decrease of the Cu–O coordination number (CN) derived from extended X-ray absorption fine structure (EXAFS) (Table S4). The XAS spectra at the Cu K edge of Cu–Zn–Y_7/silica and Cu–Zn–Y_7/MWW (both as-synthesized and after oxidation treatment) show pre-edge features and edge energies that are similar to Cu–Zn–Y_7/Beta (Figure S8A, Table S4), indicating the same Cu(II) oxidation state.

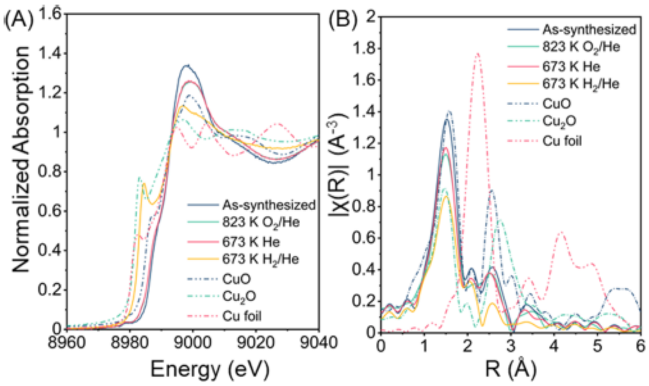

Figure 1. Cu K edge XAS spectra of Cu–Zn–Y_7/Beta as a function of thermal treatment history. (A) XANES spectra along with Cu oxide and Cu foil references. (B) k^2-Weighted Fourier-transformed (FT) EXAFS for Cu–Zn–Y_7/Beta along with CuO, Cu_2O, and Cu foil references.

After He treatment, Cu sites in Cu–Zn–Y_7/Beta remain as Cu(II) and the coordination environment does not change significantly. However, a fraction of Cu(II) in the Cu–Zn–Y_7/MWW sample is reduced to Cu(I), as indicated by the characteristic peak for Cu(I) at 8983.0 eV (Figure S8C), consistent with the decrease of fitted Cu–O CN from 4.0 to 3.2 and reduced bond length (Table S4). Cu–Zn–Y_7/silica shows more Cu(I) features after heat treatment in He (XANES analysis, Figure S8C), and the CN reduces to 2.9 (Table S4). Treatment in the reducing environment (3.5 kPa H_2/He, 673 K) leads to a 3.1 eV decrease in edge energy on Cu–Zn–Y_7/Beta, which is consistent with the reduction of some Cu(II) sites to Cu(I) with a fraction of Cu(II) sites remaining, as indicated by the 2.9 O coordinated with Cu, but no Cu–Cu scattering indicative of metallic Cu formation is observed (Figure 1B). Such treatment on Cu–Zn–Y_7/MWW continues to reduce Cu(II) to Cu(I) with a majority of the Cu sites present as Cu(I) after reduction. Metallic Cu becomes the dominant Cu species over Cu–Zn–Y_7/silica after reduction in hydrogen with some residual Cu(I) sites. Cu–Cu scattering, whether from metallic copper or second nearest neighbor copper in copper oxides, is absent, indicating that the majority of Cu sites are highly dispersed over Cu–Zn–Y_7/Beta regardless of treatments, consistent with the findings from the HAADF-STEM imaging. The lack of Cu–Cu scattering in the Cu–Zn–Y_7/MWW EXAFS spectra (Figure S8H) indicates a similar conclusion. The majority of the Cu sites over the as-received, calcined, and He-treated Cu–Zn–Y_7/silica samples are also highly dispersed, as shown in Figure S8H; however, hydrogen reduction leads to the formation of metallic Cu, as indicated by the presence of Cu–Cu coordination at 2.2 Å (phase-uncorrected distance). The difference in the reducibility of the Cu sites clearly indicates the presence of different Cu species over these supports.

XAS spectra at the Zn K edge show Zn edge energies on Cu–Zn–Y_7/Beta, Cu–Zn–Y_7/MWW, and Cu–Zn–Y_7/silica samples that are within 3.4 eV of the ZnO reference (Figures 2A,B, S9), indicating that the majority of Zn sites exist as Zn(II) species in all samples characterized here. This observation remains consistent after each of the treatment

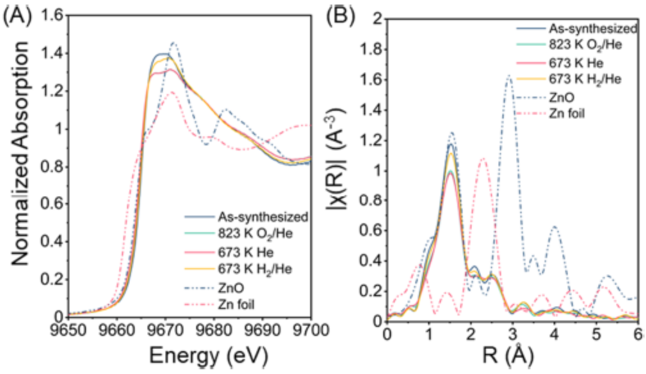

Figure 2. Zn K edge XAS spectra of Cu–Zn–Y_7/Beta as a function of thermal treatment history. (A) XANES spectra along with Zn oxide and Zn foil references. (B) k^2-Weighted FT EXAFS for Cu–Zn–Y_7/Beta along with ZnO and Zn foil references.

conditions including exposure to oxidizing and reducing environments at high temperatures (673 K). The Zn K-edge FT-EXAFS (Figures 2B and S9B,D,F,H) spectra show no peaks related to Zn−Zn scattering from either Zn metal or Zn oxide (from second nearest neighbor Zn) in the Cu−Zn−Y_7/Beta, Cu−Zn−Y_7/MWW, and Cu−Zn−Y_7/silica spectra, indicating that Zn centers on each material are also highly dispersed. Although both zeolite and silica supports provide anchoring sites to facilitate the formation of single-site Zn(II), the Zn centers over these supports are very likely to be different in their extended environments, as indicated by the difference in the XANES white line peaks after dehydration (Figure S9C,E).

At the yttrium K edge, the edge energies of Y species in the as-synthesized Cu−Zn−Y_7/Beta, Cu−Zn−Y_7/MWW, and Cu−Zn−Y_7/silica samples and those after all the subsequent treatments are similar to the Y_2O_3 reference (Figures 3 and S10, Table S6), consistent with Y(III) oxidation state. Fitting the EXAFS spectra of the as-synthesized Cu−Zn−Y_7/Beta requires the use of two Y−O bond lengths (2.26 Å at 2.9 CN and 2.41 Å at 2.8 CN) with a combined 5.7 Y−O CN. The shorter distance could be assigned to Y−O−Si and longer one to Y−O(H)Si or Y−OH_2,[42] respectively. After thermal treatment (calcination), the overall CN decreases to 4.7, with a CN of 2.4 at 2.24 Å and 2.3 at 2.39 Å, likely due to dehydration. The absence of peaks at ~3 Å (phase-uncorrected distance) reflecting scattering from the second-nearest neighbor Y (as in Y_2O_3) on Cu−Zn−Y_7/Beta (Figure 3B) suggests that Y centers are highly dispersed, and similar conclusions can be drawn from the EXAFS spectra of Cu−Zn−Y_7/MWW and Cu−Zn−Y_7/silica; however, this does not necessarily indicate the incorporation of metal species into silanol nests or the zeolitic framework. Differences in the white line and postedge peak shape between the supports suggests small differences in the local bonding environment of Y centers between these three materials. Overall, the Cu−Zn−Y_7/Beta catalyst that primarily possesses highly dispersed Cu, Zn, and Y sites with Cu sites can be reduced to Cu(I) in the reductive treatment while still maintaining predominantly single sites. Cu, Zn, and Y sites on MWW and silica supports are also highly dispersed (except Cu−Zn−Y_7/silica, which shows Cu nanoparticle formation after reduction), but individual metal centers are nonequivalent among various supports, as shown from the differences in the reducibility of various Cu sites and in the white line peaks of Zn and Y sites.

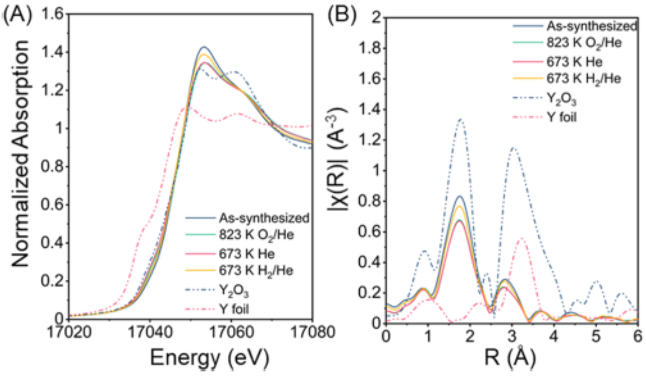

Figure 3. Y K edge XAS spectra of Cu−Zn−Y_7/Beta as a function of thermal treatment history. (A) XANES spectra along with Y oxide and Y foil references. (B) k^2-Weighted FT EXAFS for Cu−Zn−Y_7/Beta along with Y_2O_3 and Y foil references.

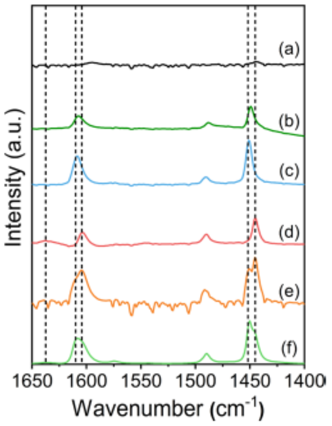

Figure 4. Transmission IR spectra collected on (a) DeAl-Beta, (b) Cu/Beta, (c) Zn/Beta, (d) Y_7/Beta, (e) Zn−Y_7/Beta, and (f) Cu−Zn−Y_7/Beta after pyridine saturation at 423 K.

To further investigate the metal-site nature on the trimetallic Cu−Zn−Y_7/Beta material, transmission IR spectra were collected on mono-, bi-, and trimetallic Beta samples after saturating with pyridine (Figure 4) to probe the presence of Lewis- and Brønsted-acid sites generated by the metal species. The spectra of Cu/Beta and Zn/Beta show two peaks centered around 1450 and 1608 cm^{-1}, which are not present over the DeAl-Beta support, reflecting the perturbed pyridine deformation modes on Lewis acid sites.[43] The lack of peaks around 1545 or 1637 cm^{-1}, assigned to protonated pyridine on Brønsted acid sites,[44] indicates that Cu and Zn species primarily induce Lewis acidity, in alignment with previous reports on CuSiBEA[39] and CIT-6 (Zn-Beta).[45] On Y/Beta, peaks at 1445 and 1603 cm^{-1} can be assigned to Lewis acid sites induced by highly dispersed Y sites. The peak at 1445 cm^{-1} could also result from hydrogen binding of pyridine to silanol groups,[46] but we separately verified that this saturation and purge treatment eliminated all absorption at 1445 cm^{-1} over dealuminated Beta and thus ascribed the peaks at 1445 cm^{-1} that remain after purging in He at 423 K pyridine bound to Lewis-acidic Y sites. Cu−Zn−Y_7/Beta preserves Lewis-acid features observed in the monometallic samples, with the primary peak at 1450 cm^{-1} and a shoulder peak at 1445 cm^{-1}. The peak centered at 1637 cm^{-1} reflects protonated pyridine species and is caused by pyridine adsorption onto Brønsted acid sites. Generally, the incorporation of trivalent metal species (*e.g.*, B^{3+}, Al^{3+}, and Ga^{3+})[47] into zeolite frameworks via isomorphous substitution with a silicon atom generates an exchangeable Brønsted acid sites to balance the framework charge. Here, the introduction of Y^{3+} into silanol nests formed during dealumination could also generate the Brønsted acid sites observed in IR spectra at 1637 cm^{-1} over Y_7/Beta.[48] The addition of Zn and/or Cu sites onto Y_7/Beta further reduces the amount of Brønsted acid sites, as indicated by the decreased IR peak area at 1637 cm^{-1}, as shown in the pyridine-saturated transmission IR analysis for Zn−Y_7/Beta and Cu−Zn−Y_7/Beta, which is potentially due to ion exchange of Y-induced Brønsted acid sites with either Cu or Zn sites. In addition, the peak intensity of the O−H stretching region (3800−3200 cm^{-1}) decreases after incorporating Y (Figure S11), which suggests metal interactions with the silanols, either

Table 1. Ethanol Conversion and Product Selectivities over Cu–Zn–Y_7/Beta, Cu–Zn–Y_7/Silica, and Cu–Zn–Y_7/MWW[a]

		selectivity (%)							
	conversion (%)	AA	DEE	ethylene	propene	butenes	butadiene	C_{5+} olefins	C_{3+} olefins
Cu–Zn–Y_7/Beta	100	1.9	0.0	9.1	5.0	66	0.0	17	88
Cu–Zn–Y_7/silica	68	23	2.6	12	1.9	31	8.7	16	49
Cu–Zn–Y_7/MWW	75	22	6.1	37	2.4	15	9.0	6.8	24

[a] Reaction conditions: 623 K, 7.1 kPa ethanol, 94.3 kPa H_2, WHSV 0.51 h^{-1}. AA, acetaldehyde; DEE, diethyl ether. The relative errors in conversion and selectivities are ±5%. Selectivities of butyraldehyde and light alkanes (methane, ethane, and propane) are not included. Butadiene selectivity is not included in total C_{3+} olefin selectivity.

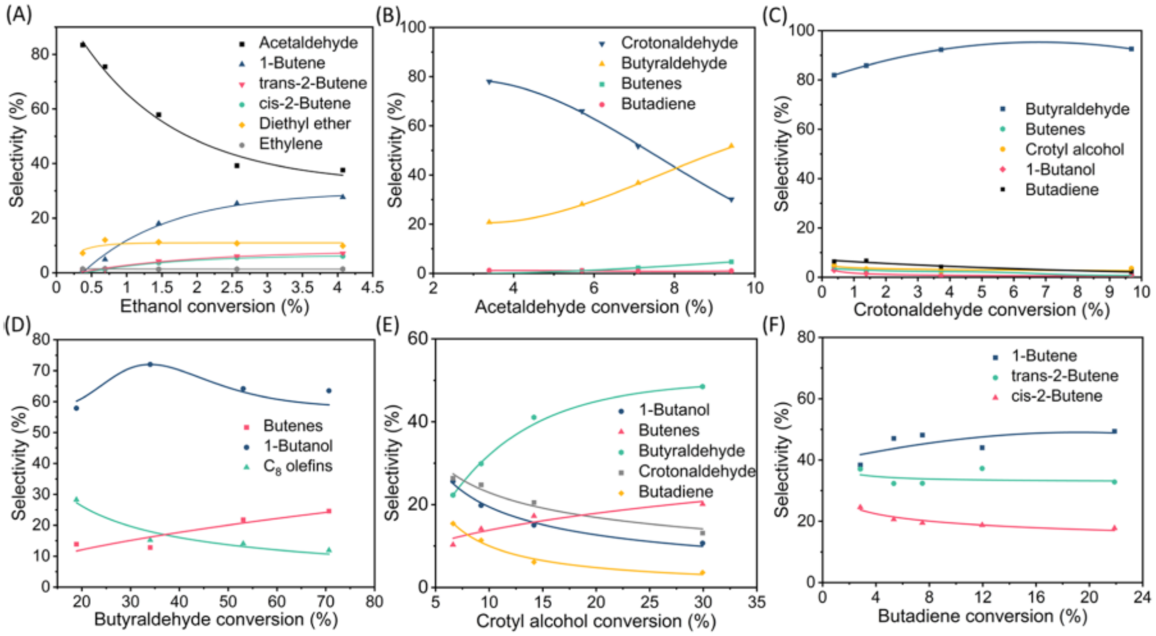

Figure 5. Selectivity plots as a function of conversion for (A) ethanol (503 K, 7.2–8.4 kPa ethanol, 97.5–112.0 kPa H_2, 0.9–16.1 h^{-1} WHSV), (B) acetaldehyde (487 K, 2.3–2.5 kPa acetaldehyde, 104.5–112.6 kPa H_2, 1.0–9.8 h^{-1} WHSV), (C) crotonaldehyde (503 K, 2.1–2.3 kPa crotonaldehyde, 109.5–119.7 kPa H_2, 3.0–29.2 h^{-1} WHSV), (D) butyraldehyde (543 K, 1.9–2.1 kPa butyraldehyde, 105.0–118.5 kPa H_2, 0.8–6.8 h^{-1} WHSV), (E) crotyl alcohol (493 K, 1.8–2.2 kPa crotyl alcohol, 1.4.8–118.4 kPa H_2, 0.8–6.8 h^{-1} WHSV), and (F) butadiene (543 K, 1.2–1.4 kPa butadiene, 27.6–32.7 kPa H_2, 1.0–12.6 h^{-1} WHSV).

via grafting onto the surface or incorporating into the framework to form Si–O–Y linkages that replace Si–O–H linkages. Altogether, these pyridine-saturated DRIFTS spectra indicate the presence of primarily Lewis-acidic Cu, Zn, and Y sites on Cu–Zn–Y_7/Beta and Y-derived Brønsted acid sites on Y/Beta, wherein the latter is decreased in the presence of Zn or Cu species.

3.2. Ethanol Conversion over Cu–Zn–Y/Beta. Ethanol conversion and product selectivities over Cu–Zn–Y_7/Beta and other trimetallic catalysts were measured under the same reaction conditions (623 K, 7.0 kPa ethanol, 94.3 kPa H_2, WHSV = 0.51 h^{-1}) for an initial comparison at high ethanol conversions, as shown in Table 1. Ethanol conversions are similar over Cu–Zn–Y_7/MWW and Cu–Zn–Y_7/silica (68–75% conversion) but are distinctly higher over Cu–Zn–Y_7/Beta (100% conversion). Similar products are formed over all three catalysts and mainly include acetaldehyde, ethylene, propene, butenes, C_{5+} olefins, and water. Notably, Cu–Zn–Y_7/Beta produces 88% butene-rich C_{3+} olefins (66% selectivity to butenes, 15% 1-butene, 30% *trans*-2-butene, and 21% *cis*-2-butene) which greatly exceeds those reported for other ethanol conversion pathways over Brønsted acid zeolites, metal oxides, and transition-metal-promoted Lewis acidic oxide catalysts[14] in single-step catalytic operations (Table S7). This increased selectivity toward C_{3+} olefins over Cu–Zn–Y_7/Beta is predominantly due to the inhibition or elimination of the reactions generating side products (*e.g.*, ethylene, aromatics, CO_2, and light paraffins). For example, the selectivity of ethylene, the main side product from ethanol dehydration, is dramatically reduced to <10%, in drastic comparison with higher ethylene selectivity in pathways that are catalyzed by Brønsted acid zeolites[49] and transition-metal-promoted Lewis acid oxides.[25] The absence of detectable CO_2 suggests the propensity of Cu–Zn–Y_7/Beta to avoid the acetone-based pathway, which is generally catalyzed by strong basic oxide catalysts (*e.g.*, $ZnZrO_x$,[23] and CeO_2,[50] as shown in Table S7). Product distributions over the other two trimetallic catalysts demonstrate lower C_{3+} olefin selectivity relative to Cu–Zn–Y_7/Beta despite similar loadings of Cu, Zn, and Y sites (Table S1). Significantly increased acetaldehyde formation over Cu–Zn–Y_7/silica and Cu–Zn–Y_7/MWW relative to Cu–Zn–Y_7/Beta indicates lower C–C coupling activity on the silica and deboronated MWW-supported catalysts. This observation of support impact on C–C coupling will be further investigated and discussed in Section 3.4. In addition, low-temperature (473–573 K) ethanol conversion experiments over Cu–Zn–Y_7/Beta yield similar product types despite different ethanol conversions and product selectivities (Table S8), suggesting a

Scheme 1. Proposed Reaction Network for Ethanol Conversion to Butenes[a]

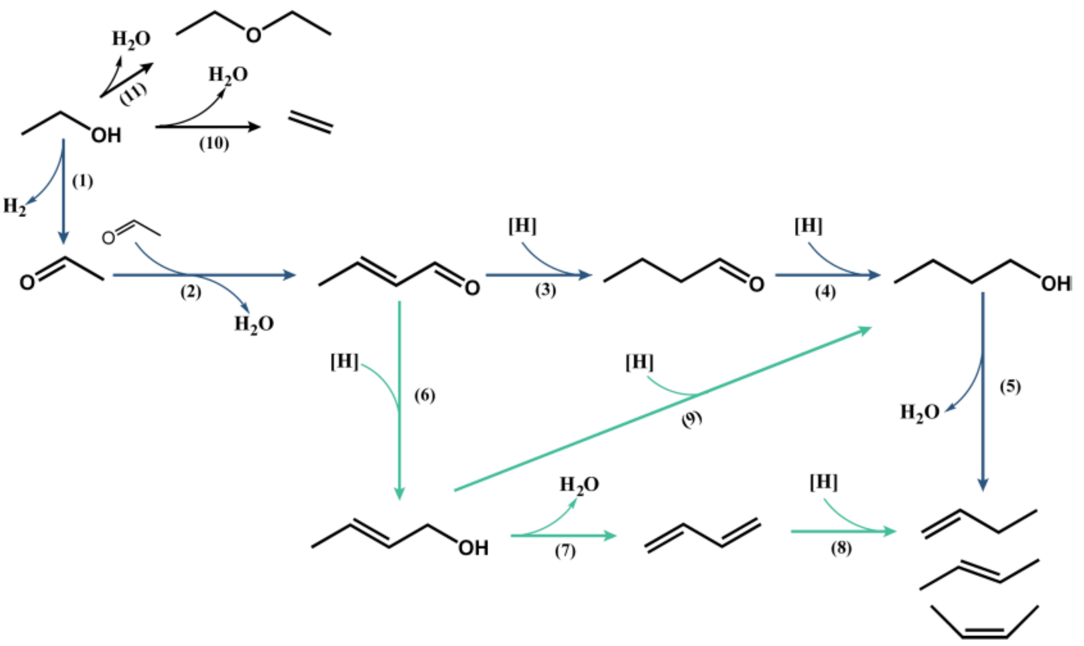

[a] [H] represents hydrogen from either gas phase H_2 or alcohol hydrogen donors. The blue lines represent the major reaction routes from ethanol to butenes. Conversion of 1-butanol is likely to form 1-butene first and can be followed by isomerization to 2-butenes. This isomerization step is not included in the scheme.

similar general reaction network at different temperatures within 473 and 623 K.

To probe the cascading reaction network that leads to the observed major olefin products (*e.g.*, butenes), ethanol and various reaction intermediates (*e.g.*, acetaldehyde, crotonaldehyde, butyraldehyde, crotyl alcohol, and butadiene) were individually fed over Cu–Zn–Y_7/Beta in the presence of hydrogen to generate selectivity–conversion relationship plots at varying space velocities (Figure 5). Ethanol is predominantly dehydrogenated to acetaldehyde over Cu–Zn–Y_7/Beta (84% selectivity at 0.4% ethanol conversion, Figure 5A), and acetaldehyde selectivity decreases as butene isomer selectivities increase at higher ethanol conversion (4%). Ethanol dehydration products, namely, ethylene and diethyl ether, are observed at all measured ethanol conversions. Experiments with acetaldehyde as the sole carbon source in the feed (Figure 5B) show crotonaldehyde as the primary product (<8% acetaldehyde conversion), presumably via aldol condensation[51] (step 2, Scheme 1). As crotonaldehyde is consumed, butyraldehyde formation gradually increases and dominates the product stream (51% selectivity) at 9.4% acetaldehyde conversion, reflecting primary hydrogenation of the C=C bond in crotonaldehyde (step 3, Scheme 1) over the Cu–Zn–Y_7/Beta catalyst. Such a phenomenon is also observed when directly feeding crotonaldehyde (Figure 5C), wherein >81% butyraldehyde selectivity is maintained at all crotonaldehyde conversions (0.4–9.7%). Feeding butyraldehyde yields 1-butanol ($\leq$ 72% selectivity at 34% conversion, Figure 5D) via carbonyl reduction (step 4, Scheme 1), and the obtained 1-butanol can be dehydrated directly into butenes (step 5, Scheme 1).

The other potential route for butene formation consists of hydrogenating the crotonaldehyde carbonyl to form crotyl alcohol (step 6, Scheme 1) either with gas phase hydrogen or through intermolecular Meerwein–Ponndorf–Verley (MPV) reduction with an alcohol as the hydrogen donor.[52] Both butyraldehyde and crotyl alcohol are observed over Cu–Zn–Y_7/Beta from crotonaldehyde conversion (82–93% selectivity for butyraldehyde and 2.3–4.8% selectivity for crotyl alcohol at 0.4–9.7% crotonaldehyde conversion, Figure 5C), reflecting competing hydrogenation reactions of the C=C and C=O bonds, respectively; however, a markedly higher selectivity toward butyraldehyde relative to crotyl alcohol is observed, which is consistent with the observation of crotonaldehyde conversion in the presence of both ethanol and hydrogen (Figure S12). Both findings indicate preferential C=C hydrogenation under the hydrogen environment, which is distinct from other reported pathways over Zn–Y/Beta[33] or Ag/ZrBeta,[26] which primarily catalyzes ethanol to butadiene formation through the reduction of crotonaldehyde to crotyl alcohol via MPV reduction with ethanol over Lewis acid sites. The presence of Cu sites over Cu–Zn–Y_7/Beta presumably favors hydrogenation of the crotonaldehyde C=C bond, leading to butyraldehyde formation.[51] The formed crotyl alcohol can be further dehydrated or hydrogenated to form butadiene (step 7, Scheme 1) or 1-butanol (step 9, Scheme 1), respectively, as both butadiene and 1-butanol selectivities continue to decrease when increasing crotyl alcohol conversion from 7 to 30% (Figure 5E). The butadiene formed from dehydration of crotyl alcohol can undergo selective hydrogenation to produce 1-butene and 2-butenes. We would like to note our primary focus is understanding the major reaction pathways to butenes (the dominant products in ethanol conversion over Cu–Zn–Y_7/Beta) and that detailed mechanistic studies of the reactions that lead to the formation of minor products (*e.g.*, propene and C_{5+} olefins) will be reported in the future.

3.3. Catalytic Functionalities of the Metal Sites over Cu–Zn–Y_7/Beta.

Equipped with the proposed reaction network (Scheme 1), the primary catalytic functionalities of

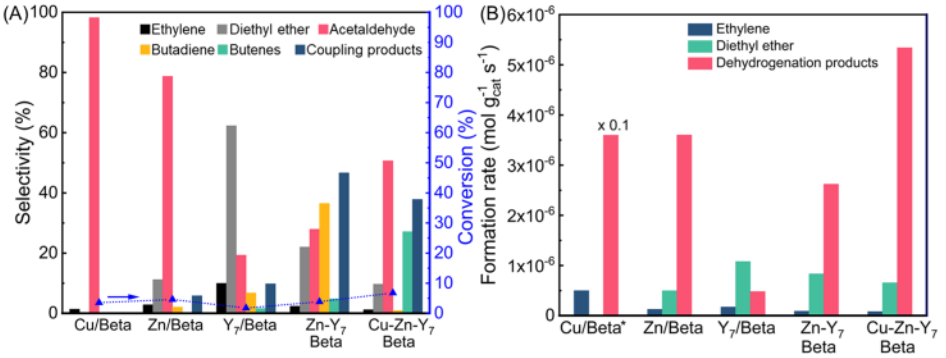

Figure 6. (A) Ethanol conversions and product selectivities and (B) product formation rates over monometallic, bimetallic, and trimetallic Beta catalysts [543 K, 8.4 kPa ethanol in 113.6 kPa H_2, WHSV = 16.0 h^{-1}, except Cu/Beta (WHSV = 172 h^{-1})]. Coupling products include butadiene, butenes, C_4 aldehydes, and C_6 olefins. The dehydrogenation products include acetaldehyde, butene, butadiene, C_4 aldehydes, and C_6 olefins. *The ethanol dehydrogenation rate over Cu/Beta is divided by 10 to allow for easier comparison.

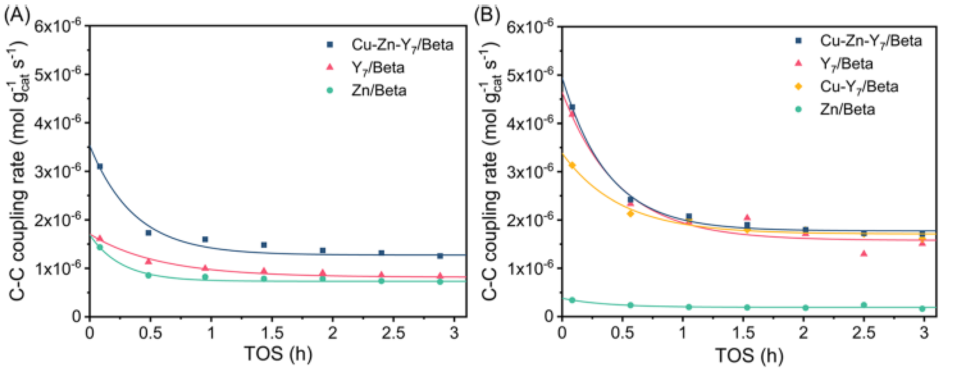

Figure 7. C−C coupling rate with (A) acetaldehyde at 543 K, total pressure 115.1, 1.2 kPa acetaldehyde, WHSV = 3.1−6.2 h^{-1}, balance H_2. (B) Acetaldehyde and ethanol at 543 K, total pressure 115.1, 1.2 kPa acetaldehyde, 12 kPa ethanol, acetaldehyde WHSV = 3.1−6.2 h^{-1}, ethanol WHSV = 33−65 h^{-1}, balance H_2.

the Cu, Zn, and Y sites were investigated by comparing the reaction rates and product selectivities at low ethanol conversions (<10%) over monometallic, bimetallic, and trimetallic Beta catalysts (543 K, 8.38 kPa ethanol, 114 kPa H_2, Figure 6). Monometallic reference samples (Cu/Beta, Zn/Beta, and Y_7/Beta) all contain isolated metal centers, as indicated by the absence of second-shell M−O−M (M = Cu, Zn, or Y) scattering peaks in the EXAFS spectra (Figure S13), similar to the results from Cu−Zn−Y_7/Beta. Both Cu/Beta and Zn/Beta predominantly form acetaldehyde (98% selectivity at 3.5% ethanol conversion over Cu/Beta and 79% selectivity at 4.6% conversion on Zn/Beta), confirming the ability of Cu and Zn sites to perform ethanol dehydrogenation, as previously reported.[23,35] Y_7/Beta mainly produces dehydration products (62% diethyl ether and 10% ethylene) along with significantly lower acetaldehyde selectivity (19%) at 1.7% ethanol conversion. Apparent dehydrogenation rates normalized per mole of metal sites reflecting combined acetaldehyde, C_4, and C_6 products formations are used to compare the dehydrogenation activities among these monometallic catalysts. Monometallic Cu/Beta catalyzes dehydrogenation at a higher rate (2.2×10^{-1} mol mol_{Cu}^{-1} s^{-1}) than Zn/Beta (1.2×10^{-2} mol mol_{Zn}^{-1} s^{-1}), while Y_7/Beta has negligible dehydrogenation reactivity per Y (6.3×10^{-4} mol mol_{Y}^{-1} s^{-1}), consistent with the low acetaldehyde selectivity observed on Y_7/Beta. The measured dehydrogenation rate per Zn site over bimetallic Zn−Y_7/Beta (0.9×10^{-2} mol mol_{Zn}^{-1} s^{-1}) is close to Zn/Beta (1.2×10^{-2} mol mol_{Zn}^{-1} s^{-1}), further indicating the insignificant contribution of Y sites to the ethanol dehydrogenation activity and suggesting that any Zn−Y ensemble sites, if present, do not significantly affect observed rates of dehydrogenation. The dehydrogenation rate over Cu−Zn−Y_7/Beta per Zn is two times higher than that over Zn−Y_7/Beta (2.1×10^{-2} vs 0.9×10^{-2} mol mol_{Zn}^{-1} s^{-1}), as expected if there is a contribution to the observed dehydrogenation activity from the Cu sites. However, the dehydrogenation rate per Cu site for Cu−Zn−Y_7/Beta is significantly lower than that for monometallic Cu/Beta (3.8×10^{-2} vs 2.2×10^{-1} mol mol_{Cu}^{-1} s^{-1}), potentially reflecting the presence of different types of Cu species in the monometallic and the trimetallic catalysts. In summary, both Cu and Zn can catalyze ethanol dehydrogenation to form acetaldehyde; however, Cu sites are likely to contribute more to the dehydrogenation activity than Zn sites over the Cu−Zn−Y_7/Beta catalyst.

When combining Y sites with Zn sites, C−C coupling products become dominant, as reflected in butadiene-rich product distributions over Zn−Y_7/Beta (37% butadiene and 5% butene selectivities, Figure 6A) in comparison with all the monometallic catalysts, potentially suggesting that Y-containing sites catalyze aldol condensation reaction(s). To further understand the role of the various metals in aldol condensation, C−C coupling rates, reflecting the combined formation rates of C_4 and C_6 products, were measured by feeding either acetaldehyde (Figure 7A) or an acetaldehyde−ethanol mixture (Figure 7B). The initial C−C coupling rates normalized by the gram of catalyst with acetaldehyde as the

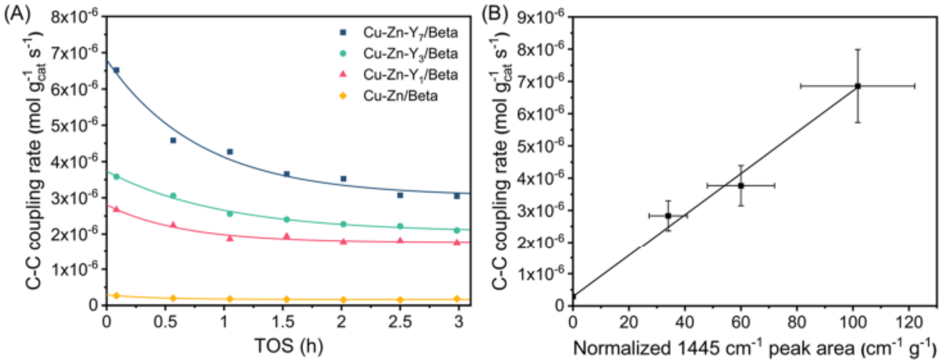

Figure 8. (A) C−C coupling rates over Cu−Zn−Y/Beta with varying Y loading (543 K, total pressure 115.1 kPa, 0.8 kPa acetaldehyde, 7.9 kPa ethanol balanced with H_2, acetaldehyde WHSV = 2.1−4.2 h^{-1}, ethanol WHSV = 22−42 h^{-1}). (B) Initial C−C coupling rate as a function of Lewis-acidic Y site density. Quantification of Lewis-acidic Y sites is performed by pyridine FTIR and shown in Figure S18 and Table S9.

sole organic reactant (543 K, 1.2 kPa acetaldehyde, balance H_2) are 1.7×10^{-6}, 1.7×10^{-6}, and 3.5×10^{-6} mol g_{cat}^{-1} s^{-1} for Zn/Beta, Y_7/Beta, and Cu−Zn−Y_7/Beta, respectively, indicating that both Zn and Y sites contribute to acetaldehyde aldol condensation to crotonaldehyde (Figures S14 and S15). It is worth noting that the initial C−C coupling rates normalized by mole of metal sites indicate that Zn/Beta is more reactive than Y_7/Beta (5.5×10^{-3} mol mol_{Zn}^{-1} s^{-1} vs 2.3×10^{-3} mol mol_Y^{-1} s^{-1}) when acetaldehyde is the sole organic reactant. Both Zn and Y sites are not effective for hydrogenation of crotonaldehyde to either butyraldehyde or crotyl alcohol in the presence of acetaldehyde and hydrogen, as reflected by low selectivities and formation rates to these hydrogenation products and any associated downstream products (*e.g.*, butadiene and butenes), as shown in Figures S14 and S15. The introduction of Cu sites increases the initial formation rate of butyraldehyde over Cu−Zn−Y_7/Beta to 1.4×10^{-6} mol g_{cat}^{-1} s^{-1} (in comparison with 7.6×10^{-8} mol g_{cat}^{-1} s^{-1} over Zn/Beta and 7.6×10^{-8} mol g_{cat}^{-1} s^{-1} over Y_7/Beta, Figure S14), further reflecting the role of Cu in promoting the hydrogenation of the C═C bond in crotonaldehyde.

In the low-ethanol-conversion experiments (<10% conversion, Figure 6), the partial pressure ratio of ethanol and acetaldehyde in the final product stream is >10, so cofeeding of ethanol with acetaldehyde (543 K, 12 kPa ethanol, 1.2 kPa acetaldehyde, balance with H_2, Figure 7B) was performed to measure the C−C coupling rates to mimic the low ethanol conversion scenarios and understand the impact of ethanol on the coupling activities of the metal centers (product formation rates and selectivities are shown in Figures S16 and S17). The initial C−C coupling rate over Zn/Beta decreases to 0.4×10^{-6} mol g_{cat}^{-1} s^{-1}, which is much lower than that measured in the presence of just acetaldehyde and hydrogen reactants (1.7×10^{-6} mol g_{cat}^{-1} s^{-1}, Figure 7A), suggesting that either ethanol or ethanol-derived products (*e.g.*, butadiene and C_4 alcohols) inhibit condensation reactions over Zn. The initial C−C coupling rates over Y_7/Beta, Cu−Y_7/Beta, and Cu−Zn−Y_7/Beta are 4.6×10^{-6}, 3.4×10^{-6}, and 4.9×10^{-6} mol g_{cat}^{-1} s^{-1} (543 K, 12 kPa ethanol, 1.2 kPa acetaldehyde, balance with H_2, Figure 7B), respectively, suggesting Y-induced sites play the primary role in the coupling reactions and that Zn sites provide slight promotion of C−C coupling rates, as reflected by the increase of coupling rates from 3.4 to 4.9×10^{-6} mol g_{cat}^{-1} s^{-1} (Cu−Y_7/Beta vs Cu−Zn−Y_7/Beta). Cofeeding ethanol with acetaldehyde increases overall C−C coupling rates, potentially suggesting the direct coupling of ethanol and acetaldehyde over Y sites as recently reported.[34]

The addition of Cu sites onto Zn−Y_7/Beta (Cu−Zn−Y_7/Beta) leads to a shift of the product selectivity from a high butadiene to butene ratio (37% butadiene and 5% butenes over Zn−Y_7/Beta) to a high butene to butadiene ratio (27% butenes and 1% butadiene over Cu−Zn−Y_7/Beta) (543 K, 8.4 kPa ethanol in balance H_2, Figure 6A), which can be attributed to either increased hydrogenation of the C═C bond on crotonaldehyde to form butyraldehyde or to selective hydrogenation of butadiene over Cu sites. The former has been demonstrated during experiments with crotonaldehyde and hydrogen in the feed stream (Figure 5C) where butyraldehyde is the major product that results from hydrogenation of crotonaldehyde over Cu−Zn−Y_7/Beta. An increased butyraldehyde formation rate is observed on Cu−Zn−Y_7/Beta compared with Zn/Beta and Y_7/Beta when the feed comprises acetaldehyde (1.2 kPa) and hydrogen (113.9 kPa, Figure S14), reflecting the role of Cu sites in hydrogenating the C═C bond in crotonaldehyde, potentially with gas-phase hydrogen. Based on these observations, the major catalytic functionalities of these metal centers within the ethanol-to-butene reaction network can be evinced. On Cu−Zn−Y_7/Beta, both Cu and Zn contribute to ethanol dehydrogenation, Y sites catalyze aldol condensation (with slight contribution to aldol condensation from Zn sites), and Cu sites perform intermediate hydrogenation steps (particularly crotonaldehyde to butyraldehyde) in the presence of hydrogen.

As multiple types of Y sites (*e.g.*, Lewis acid sites and Brønsted acid sites) have been observed based on the pyridine transmission IR studies, understanding which Y sites are relevant to aldol condensation is essential for improved catalyst design. Figure 8A shows the C−C coupling rates over dealuminated Beta supported trimetallic catalysts with varying Y loadings from 0 to 7.0 wt % (543 K, total pressure 115.1 kPa, 0.8 kPa acetaldehyde, 7.9 kPa ethanol with balance H_2). C−C coupling rates increase with Y loading at all times on stream, which qualitatively indicates that Y sites promote the coupling reactions, consistent with the findings from Figure 7B. To quantitively understand the relationship between coupling activity and catalyst acidity, transmission IR spectra were collected over all the Cu−Zn−Y/Beta samples with varying Y loadings after pyridine saturation, as shown in Figure S18. Due to the absence of reported integrated molar extinction coefficients (IMECs) for pyridine bound to Lewis-acidic Y sites, integrated peak areas (for the peak centered at 1445

https://doi.org/10.1021/acscatal.1c02177
ACS Catal. 2021, 11, 9885−9897

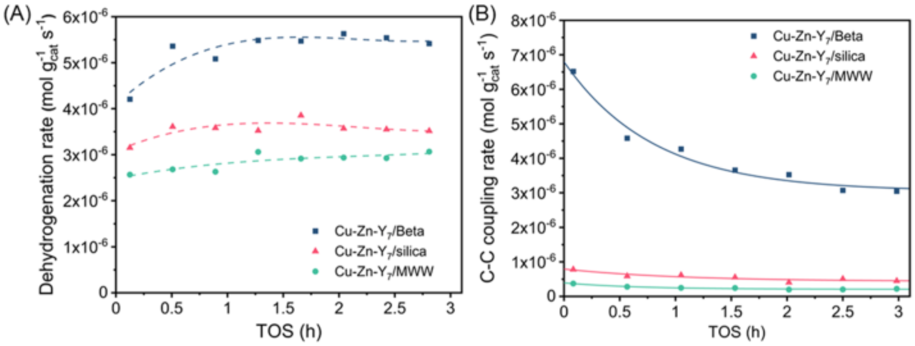

Figure 9. (A) Ethanol dehydrogenation rates (543 K, 8.4 kPa ethanol in balance H_2, WHSV = 16.0 h^{-1}) and (B) C–C coupling rates over Cu–Zn–Y_7/Beta, Cu–Zn–Y_7/silica, and Cu–Zn–Y_7/MWW (543 K, total pressure 115.1 kPa, 0.8 kPa acetaldehyde, 7.9 kPa ethanol balanced with H_2, acetaldehyde WHSV = 2.1–4.2 h^{-1}, ethanol WHSV = 22–42 h^{-1}). Lines in (A) are used to guide the eye.

cm^{-1}) normalized by catalyst wafer mass rather than moles of Lewis-acidic Y sites, are used to allow comparisons of the density of Lewis-acidic Y sites across a series of samples (Table S9). A linear dependence of the initial C–C bond formation rates per catalyst weight as a function of normalized FTIR peak areas for pyridine bound to Lewis-acidic Y sites is observed (Figure 8B), suggesting that Lewis-acidic Y sites are the predominant sites that catalyze C–C coupling in Cu–Zn–Y/Beta catalysts. Besides the apparent significance of Lewis-acidic Y sites, we cannot completely rule out the contributions from other types of Y sites such as the potential role of Zn–Y or Cu–Y ensemble sites, or Y sites that do not bind pyridine strongly and cannot be directly probed by adsorption of pyridine and collection of FTIR spectra. It is also challenging to provide further insights into the structure of the Lewis-acidic Y sites or to rule out the possibility of multiple types of Y Lewis-acid sites with similar local coordination, as have been reported previously for metal-containing Beta zeolites.[53,54] Further studies of the local structure of Y sites using more sensitive techniques than pyridine chemisorption coupled with FTIR are required to develop a more detailed understanding of these sites.

In summary, we have illustrated the primary catalytic functionalities of the metal sites within the proposed ethanol-to-butene reaction network (Scheme 1). Both Cu and Zn sites are likely to contribute to ethanol dehydrogenation to acetaldehyde, but Cu sites are likely more reactive for dehydrogenation than Zn sites. Aldol condensation of acetaldehyde is primarily catalyzed by Lewis-acidic Y sites, while Zn sites show slight promotion of the C–C coupling rate when feeding a mixture of ethanol andacetaldehyde. The presence of Cu sites favors the hydrogenation of the C═C bond in crotonaldehyde, which leads to the formation of butyraldehyde, a key distinction from the conventional ethanol to butadiene route over Zn–Y/Beta catalysts that occurs via a crotyl alcohol intermediate.[52] Since the metal sites each play important roles in the ethanol-to-butene reaction, it is intriguing to understand how the support affects the chemical nature of the metal sites and further influences the ethanol upgrading chemistry, particularly the impact on the aldol condensation activities, which has been indicated by the different selectivities of acetaldehyde and C_{3+} olefins shown in the high ethanol conversion experiments over various supported trimetallic catalysts (*i.e.*, Cu–Zn–Y/Beta, Cu–Zn–Y/silica, and Cu–Zn–Y/MWW) in Table 1. Further studies of the support impact on the metal sites and the C–C coupling activity is reported in the following section.

3.4. Support Impact on Y Sites and C–C Coupling Activities. Cu, Zn, and Y sites over various supports (dealuminated Beta, deboronated MWW, and amorphous silica) have been shown to be primarily highly dispersed, but potential differences in the structures of the metal sites could exist, as shown in the different Cu site reducibility and differences in white line peaks for Zn and Y sites based on the XAS results (Section 3.1). To further probe the reactivities of these sites (particularly Lewis-acidic Y sites that catalyze C–C coupling) over different supports and demonstrate the unique proclivity of Cu–Zn–Y_7/Beta catalysts to form butene-rich C_{3+} olefins in ethanol upgrading catalysis, reaction rates, and product selectivities at low ethanol conversions were explored over these catalysts within the context of the proposed ethanol-to-butenes reaction network outlined in Scheme 1. Products formed over Cu–Zn–Y_7/MWW and Cu–Zn–Y_7/silica are similar to those observed on Cu–Zn–Y_7/Beta, despite different product selectivities (543 K, 8.4 kPa ethanol, 133.6 kPa H_2, WHSV = 16.9 h^{-1}, Figure S19), consistent with the observations at high ethanol conversions (Table 1). Acetaldehyde is the dominant product over all these catalysts, but the ethanol dehydrogenation rate over Cu–Zn–Y_7/Beta is slightly higher than the other two catalysts (Figure 9A), potentially due to differences in the identities of the Cu and Zn sites, as indicated by the XANES analyses (Section 3.1). Further discrepancies are observed in the coupling products, as indicated by higher selectivities of butenes and butadiene over Cu–Zn–Y_7/Beta in comparison with other catalysts (Figure S19). C–C coupling rates over these catalysts are further investigated by cofeeding ethanol and acetaldehyde under differential conversions for both ethanol and acetaldehyde (543 K, 0.8 kPa acetaldehyde, 7.9 kPa ethanol, balance with H_2, Figures 9B and S20). The initial C–C coupling rate over Cu–Zn–Y_7/Beta normalized by catalyst weight (6.9×10^{-6} mol g_{cat}^{-1} s^{-1}) is nine times and 17 times higher than Cu–Zn–Y_7/silica and Cu–Zn–Y_7/MWW, respectively (0.8×10^{-6} and 0.4×10^{-6} mol g_{cat}^{-1} s^{-1}). The remarkable differences in C–C coupling rates (normalized by either catalyst weight or mole of Y sites shown in Figure S20) suggest variations in either Lewis-acidic Y-site densities or Lewis-acidic Y-site types over these different supports, the latter of which can reflect differences in either Lewis acid strength or in the confining environment around kinetically relevant sites.

To investigate the differences in Lewis-acidic Y-site densities on these materials, transmission IR spectra were collected after saturation with pyridine, as shown in Figure S21. The normalized integrated peak areas (per gram catalyst) derived from deconvoluting the peak centered at 1445 cm^{-1} reflecting pyridine bound to Lewis-acidic Y sites are compared directly as a reflection of Lewis acid densities among all three trimetallic catalysts (Table S10). Direct comparison of normalized integrated peak areas assumes a constant IMEC value across the topologies studied here, as has been investigated for Ti[55] and Sn[56] Lewis acid sites with consistent site speciation yet different confining environments. The normalized peak area of Y induced Lewis acid sites for Cu−Zn−Y_7/Beta is 106 cm^{-1} g^{-1}, while deboronated MWW and amorphous silica-supported samples have peak areas of 10 and 14 cm^{-1} g^{-1}, respectively (Table S10). Despite containing similar Y loadings (Table S1) and atomic dispersion of Y sites across all samples with similar Y−O CNs (Table S6) based on the XAS analyses, a significantly higher Y Lewis-acid-site density is shown on Cu−Zn−Y_7/Beta relative to the other trimetallic catalysts. Such distinctions in Lewis-acid Y-site density might be one of the reasons responsible for the differences in the observed C−C coupling reactivity, as shown in Figure S22, where Cu−Zn−Y_7/MWW and Cu−Zn−Y_7/silica follow the general trend of C−C coupling rate change as a function of Lewis-acid Y-site density. We cannot completely exclude other possibilities for the reactivity difference among these catalysts, such as the generation of different types of Lewis-acidic Y sites, pore confinement effects, or distinct accessibility of the Lewis-acidic Y sites. Further investigations will require additional Y-site characterizations (*e.g.*, Y solid-state NMR[57]) along with computational modeling and more controlled synthesis of Y sites over different supports, which is beyond the scope of this study and the topic of our ongoing research. Nevertheless, these findings demonstrate that different supports (dealuminated Beta, deboronated MWW, amorphous silica) can form isolated Y sites with similar Y−O CNs, but the pyridine-accessible Lewis-acid Y-site densities are significantly lower on deboronated MWW and silica supports than that for Cu−Zn−Y_7/Beta, leading to lower C−C coupling activities and lower selectivities of targeted butene-rich C_{3+} olefins when supports other than dealuminated Beta are employed.

4. CONCLUSIONS

The combination of Cu, Zn, and Y sites incorporated into the dealuminated Beta supports generates a trimetallic catalyst capable of selectively generating butene-rich C_{3+} olefins from ethanol (88% selectivity at 100% ethanol conversion, 623 K). Metal centers remain highly dispersed even when the Y loading is up to 7.0 wt % based on the XAS and HAADF-STEM analyses. This catalyst catalyzes ethanol conversion to butenes via a pathway wherein Cu sites are primarily involved in the ethanol dehydrogenation and downstream hydrogenation reactions (particularly hydrogenating the C=C bond of crotonaldehyde); Zn sites contribute to ethanol dehydrogenation and slightly promote aldol condensation, and Lewis-acidic Y sites are the predominant sites responsible for aldol condensation. Formation of butyraldehyde is dominant during crotonaldehyde hydrogenation in the presence of hydrogen, which is different from the crotyl alcohol-based ethanol to butadiene reaction pathway.

Besides the significant roles of these trimetallic sites in the ethanol-to-butene reaction, the support also influences the chemical nature of the isolated metal sites. For example, the Cu sites in silica and deboronated MWW supports show very different resistance to reduction in comparison with those in dealuminated Beta-supports. The Y sites over various supports are all highly dispersed; however, the induced Lewis acid site densities vary by up to a factor of ∼10, with Cu−Zn−Y/Beta showing the largest amount of Lewis-acidic Y sites. The differences in metal sites over different supports have led to different reactivities in the related reaction steps, for example, the initial C−C coupling rate over Cu−Zn−Y_7/Beta normalized by catalyst weight is 17 times higher than that over Cu−Zn−Y_7/MWW. The unique combination of Cu, Zn, and Y sites with Beta supports leads to the selective production of butene-rich C_{3+} olefins from ethanol.

■ ASSOCIATED CONTENT

Supporting Information

The Supporting Information is available free of charge at https://pubs.acs.org/doi/10.1021/acscatal.1c02177.

> XRD patterns, N_2 adsorption isotherms, STEM images and EDS analysis, additional XANES, EXAFS, and associated fitting results, additional pyridine saturated transmission IR spectra and normalized peak areas, additional plots of conversion, product distribution, and rate measurement (PDF)

■ AUTHOR INFORMATION

Corresponding Author

Zhenglong Li − *Oak Ridge National Laboratory, Oak Ridge, Tennessee 37830, United States;* orcid.org/0000-0001-8811-8625; Email: liz3@ornl.gov

Authors

Junyan Zhang − *Oak Ridge National Laboratory, Oak Ridge, Tennessee 37830, United States; University of Maryland, College Park, Maryland 20742, United States*

Evan C. Wegener − *Argonne National Laboratory, Lemont, Illinois 60439, United States*

Nohor River Samad − *The University of Alabama, Tuscaloosa, Alabama 35487, United States*

James W. Harris − *The University of Alabama, Tuscaloosa, Alabama 35487, United States;* orcid.org/0000-0001-6760-9951

Kinga A. Unocic − *Oak Ridge National Laboratory, Oak Ridge, Tennessee 37830, United States*

Lawrence F. Allard − *Oak Ridge National Laboratory, Oak Ridge, Tennessee 37830, United States*

Stephen Purdy − *Oak Ridge National Laboratory, Oak Ridge, Tennessee 37830, United States;* orcid.org/0000-0002-9870-1029

Shiba Adhikari − *Oak Ridge National Laboratory, Oak Ridge, Tennessee 37830, United States*

Michael J. Cordon − *Oak Ridge National Laboratory, Oak Ridge, Tennessee 37830, United States*

Jeffrey T. Miller − *Purdue University, West Lafayette, Indiana 47907, United States;* orcid.org/0000-0002-6269-0620

Theodore R. Krause − *Argonne National Laboratory, Lemont, Illinois 60439, United States*

Sichao Cheng − *University of Maryland, College Park, Maryland 20742, United States*

Dongxia Liu − *University of Maryland, College Park, Maryland 20742, United States;* orcid.org/0000-0001-8712-2219

Meijun Li − *Oak Ridge National Laboratory, Oak Ridge, Tennessee 37830, United States*

Xiao Jiang − *Oak Ridge National Laboratory, Oak Ridge, Tennessee 37830, United States*
Zili Wu − *Oak Ridge National Laboratory, Oak Ridge, Tennessee 37830, United States;* orcid.org/0000-0002-4468-3240

Complete contact information is available at:
https://pubs.acs.org/10.1021/acscatal.1c02177

Author Contributions

The manuscript was written through contributions of all authors. All authors have given approval to the final version of the manuscript.

Funding

This research is sponsored by the U.S. Department of Energy (DOE), Office of Energy Efficiency and Renewable Energy, BioEnergy Technologies Office, under contract DE-AC05-00OR22725 with UT-Battelle, LLC, and in collaboration with the Chemical Catalysis for Bioenergy (ChemCatBio) Consortium, a member of the Energy Materials Network. J.T.M was supported in part by the National Science Foundation under Cooperative Agreement No. EEC-1647722. N.R.S. and J.W.H. were supported in part by The University of Alabama Office of Research and Economic Development's Small Grants Program. Argonne National Laboratory's work was supported by the U.S. Department of Energy, Office of Energy Efficiency and Renewable Energy, Bioenergy Technologies Office, under contract DE-AC02-06CH11357. This work used the resources of the Advanced Photon Sources, which is a U.S. Department of Energy, Office of Science User Facility supported under contract DE AC02 06CH11357. MRCAT operations are supported by the Department of Energy and its member institutions. The work of X.J. and Z.W. was supported by the Center for Understanding and Control of Acid Gas-Induced Evolution of Materials for Energy (UNCAGE-ME), an Energy Frontier Research Center funded by U.S. Department of Energy, Office of Science, Basic Energy Sciences. A portion of the research was conducted at Center for Nanophase Materials Sciences, a US DOE Office of Science User Facility. The views and opinions of the authors expressed herein do not necessarily state or reflect those of the United States Government or any agency thereof.

Notes

The authors declare the following competing financial interest(s): Patent application is pending for the inventor Zhenglong Li.

This manuscript has been authored in part by UT-Battelle, LLC, under contract DE-AC05-00OR22725 with the US Department of Energy (DOE). The US government retains and the publisher, by accepting the article for publication, acknowledges that the US government retains a nonexclusive, paid-up, irrevocable, worldwide license to publish or reproduce the published form of this manuscript, or allow others to do so, for US government purposes. DOE will provide public access to these results of federally sponsored research in accordance with the DOE Public Access Plan (http://energy.gov/downloads/doe-public-access-plan).

ACKNOWLEDGMENTS

The authors acknowledge Shawn K. Reeves for assistance with transmission electron microscopy work.

REFERENCES

(1) Torres Galvis, H. M.; de Jong, K. P. Catalysts for production of lower olefins from synthesis gas: a review. *ACS Catal.* 2013, 3, 2130−2149.

(2) Hu, B.; Frueh, S.; Garces, H. F.; Zhang, L.; Aindow, M.; Brooks, C.; Kreidler, E.; Suib, S. L. Selective hydrogenation of CO_2 and CO to useful light olefins over octahedral molecular sieve manganese oxide supported iron catalysts. *Appl. Phys. B* 2013, *132-133*, 54−61.

(3) Liu, Y.; Chen, J.-F.; Bao, J.; Zhang, Y. Manganese-modified Fe_3O_4 microsphere catalyst with effective active phase of forming light olefins from syngas. *ACS Catal.* 2015, *5*, 3905−3909.

(4) Bender, M. An Overview of Industrial Processes for the Production of Olefins - C_4 Hydrocarbons. *ChemBioEng Rev.* 2014, *1*, 136−147.

(5) Bruijnincx, P. C. A.; Weckhuysen, B. M. Shale gas revolution: an opportunity for the production of biobased chemicals? *Angew. Chem., Int. Ed.* 2013, *52*, 11980−11987.

(6) Amghizar, I.; Vandewalle, L. A.; Van Geem, K. M.; Marin, G. B. New trends in olefin production. *Engineering* 2017, *3*, 171−178.

(7) Ren, T.; Patel, M. K.; Blok, K. Steam cracking and methane to olefins: Energy use, CO_2 emissions and production costs. *Energy* 2008, *33*, 817−833.

(8) Amghizar, I.; Dedeyne, J. N.; Brown, D. J.; Marin, G. B.; Van Geem, K. M. Sustainable innovations in steam cracking: CO_2 neutral olefin production. *React. Chem. Eng.* 2020, *5*, 239−257.

(9) Zheng, Q.; Wales, M. D.; Heidlage, M. G.; Rezac, M.; Wang, H.; Bossmann, S. H.; Hohn, K. L. Conversion of 2, 3-butanediol to butenes over bifunctional catalysts in a single reactor. *J. Catal.* 2015, *330*, 222−237.

(10) Adhikari, S. P.; Zhang, J.; Guo, Q.; Unocic, K. A.; Tao, L.; Li, Z. A hybrid pathway to biojet fuel via 2, 3-butanediol. *Sustainable Energy Fuels* 2020, *4*, 3904−3914.

(11) Annual Fuel Ethanol Production U.S. and World Ethanol Production. https://ethanolrfa.org/statistics/annual-ethanol-production/ (accessed 01/24/2021).

(12) Spivey, J. J.; Egbebi, A. Heterogeneous catalytic synthesis of ethanol from biomass-derived syngas. *Chem. Soc. Rev.* 2007, *36*, 1514−1528.

(13) Lee, S.; Park, G.; Lee, J. Importance of Ag−Cu biphasic boundaries for selective electrochemical reduction of CO_2 to ethanol. *ACS Catal.* 2017, *7*, 8594−8604.

(14) Eagan, N. M.; Kumbhalkar, M. D.; Buchanan, J. S.; Dumesic, J. A.; Huber, G. W. Chemistries and processes for the conversion of ethanol into middle-distillate fuels. *Nat. Rev. Chem.* 2019, *3*, 223−249.

(15) Lilga, M. A.; Hallen, R. T.; Albrecht, K. O.; Cooper, A. R.; Frye, J. G.; Ramasamy, K. K. Systems and processes for conversion of ethylene feedstocks to hydrocarbon fuels, U.S. Patent US9771533B2, September, 2017, *26*.

(16) Yuk, S. F.; Lee, M.-S.; Collinge, G.; Zhang, J.; Padmaperuma, A. B.; Li, Z.; Polo-Garzon, F.; Wu, Z.; Glezakou, V.-A.; Rousseau, R. Mechanistic Understanding of Catalytic Conversion of Ethanol to 1-Butene over 2D-Pillared MFI Zeolite. *J. Phys. Chem. C* 2020, *124*, 28437−28447.

(17) Hannon, J. R.; Lynd, L. R.; Andrade, O.; Benavides, P. T.; Beckham, G. T.; Biddy, M. J.; Brown, N.; Chagas, M. F.; Davison, B. H.; Foust, T.; Junqueira, T. L.; Laser, M. S.; Li, Z.; Richard, T.; Tao, L.; Tuskan, G. A.; Wang, M.; Woods, J.; Wyman, C. E. Technoeconomic and life-cycle analysis of single-step catalytic conversion of wet ethanol into fungible fuel blendstocks. *Proc. Natl. Acad. Sci. U.S.A.* 2020, *117*, 12576−12583.

(18) Li, Z.; Lepore, A. W.; Salazar, M. F.; Foo, G. S.; Davison, B. H.; Wu, Z.; Narula, C. K. Selective conversion of bio-derived ethanol to renewable BTX over Ga-ZSM-5. *Green Chem.* 2017, *19*, 4344−4352.

(19) Kozlowski, J. T.; Davis, R. J. Heterogeneous catalysts for the Guerbet coupling of alcohols. *ACS Catal.* 2013, *3*, 1588−1600.

(20) Berteau, P.; Delmon, B. Modified Aluminas : Relationship between activity in 1-butanol dehydration and acidity measured by NH_3 TPD. *Catal. Today* 1989, *5*, 121−137.

(21) John, M.; Alexopoulos, K.; Reyniers, M.-F.; Marin, G. B. First-principles kinetic study on the effect of the zeolite framework on 1-butanol dehydration. *ACS Catal.* 2016, *6*, 4081−4094.

(22) Zonetti, P. C.; Bridi, V. L.; Gonzalez, G. G.; Moreira, C. R.; Alves, O. C.; de Avillez, R. R.; Appel, L. G. Isobutene from Ethanol: Describing the Synergy between In_2O_3 and m-ZrO_2. *ChemCatChem* 2019, *11*, 4011−4020.

(23) Sun, J.; Zhu, K.; Gao, F.; Wang, C.; Liu, J.; Peden, C. H. F.; Wang, Y. Direct Conversion of Bio-ethanol to Isobutene on Nanosized $Zn_xZr_yO_z$ Mixed Oxides with Balanced Acid-Base Sites. *J. Am. Chem. Soc.* 2011, *133*, 11096−11099.

(24) Rorrer, J. E.; Toste, F. D.; Bell, A. T. Mechanism and Kinetics of Isobutene Formation from Ethanol and Acetone over $Zn_xZr_yO_z$. *ACS Catal.* 2019, *9*, 10588−10604.

(25) Dagle, V. L.; Winkelman, A. D.; Jaegers, N. R.; Saavedra-Lopez, J.; Hu, J.; Engelhard, M. H.; Habas, S. E.; Akhade, S. A.; Kovarik, L.; Glezakou, V.-A.; Rousseau, R.; Wang, Y.; Dagle, R. A. Single-Step Conversion of Ethanol to n-Butene over Ag-ZrO_2/SiO_2 Catalysts. *ACS Catal.* 2020, *10*, 10602−10613.

(26) Sushkevich, V. L.; Ivanova, I. I. Ag-Promoted ZrBEA Zeolites Obtained by Post-Synthetic Modification for Conversion of Ethanol to Butadiene. *ChemSusChem* 2016, *9*, 2216−2225.

(27) Palagin, D.; Sushkevich, V. L.; Ivanova, I. I. C-C Coupling Catalyzed by Zeolites: Is Enolization the Only Possible Pathway for Aldol Condensation? *J. Phys. Chem. C* 2016, *120*, 23566−23575.

(28) Kyriienko, P. I.; Larina, O. V.; Popovych, N. O.; Soloviev, S. O.; Millot, Y.; Dzwigaj, S. Effect of the niobium state on the properties of NbSiBEA as bifunctional catalysts for gas- and liquid-phase tandem processes. *J. Mol. Catal. A: Chem.* 2016, *424*, 27−36.

(29) Pomalaza, G.; Arango Ponton, P.; Capron, M.; Dumeignil, F. Ethanol-to-butadiene: the reaction and its catalysts. *Catal. Sci. Technol.* 2020, *10*, 4860−4911.

(30) Yan, T.; Yao, S.; Dai, W.; Wu, G.; Guan, N.; Li, L. Self-aldol condensation of aldehydes over Lewis acidic rare-earth cations stabilized by zeolites. *Chin. J. Catal.* 2021, *42*, 595−605.

(31) De Baerdemaeker, T.; Feyen, M.; Müller, U.; Yilmaz, B.; Xiao, F.-S.; Zhang, W.; Yokoi, T.; Bao, X.; Gies, H.; De Vos, D. E. Bimetallic Zn and Hf on Silica Catalysts for the Conversion of Ethanol to 1,3-Butadiene. *ACS Catal.* 2015, *5*, 3393−3397.

(32) Saville, B. The Concept of Hard and Soft Acids and Bases as Applied to Multi-Center Chemical Reactions. *Angew. Chem., Int. Ed.* 1967, *6*, 928−939.

(33) Dai, W.; Zhang, S.; Yu, Z.; Yan, T.; Wu, G.; Guan, N.; Li, L. Zeolite structural confinement effects enhance one-pot catalytic conversion of ethanol to butadiene. *ACS Catal.* 2017, *7*, 3703−3706.

(34) Qi, L.; Zhang, Y.; Conrad, M. A.; Russell, C. K.; Miller, J.; Bell, A. T. Ethanol Conversion to Butadiene over Isolated Zinc and Yttrium Sites Grafted onto Dealuminated Beta Zeolite. *J. Am. Chem. Soc.* 2020, *142*, 14674−14687.

(35) Hanukovich, S.; Dang, A.; Christopher, P. Influence of Metal Oxide Support Acid Sites on Cu-Catalyzed Nonoxidative Dehydrogenation of Ethanol to Acetaldehyde. *ACS Catal.* 2019, *9*, 3537−3550.

(36) Jones, M. D.; Keir, C. G.; Iulio, C. D.; Robertson, R. A. M.; Williams, C. V.; Apperley, D. C. Investigations into the conversion of ethanol into 1,3-butadiene. *Catal. Sci. Technol.* 2011, *1*, 267−272.

(37) Herrmann, S.; Iglesia, E. Elementary steps in acetone condensation reactions catalyzed by aluminosilicates with diverse void structures. *J. Catal.* 2017, *346*, 134−153.

(38) Levenspiel, O. Experimental search for a simple rate equation to describe deactivating porous catalyst particles. *J. Catal.* 1972, *25*, 265−272.

(39) Dzwigaj, S.; Janas, J.; Gurgul, J.; Socha, R. P.; Shishido, T.; Che, M. Do Cu (II) ions need Al atoms in their environment to make CuSiBEA active in the SCR of NO by ethanol or propane? A spectroscopy and catalysis study. *Appl. Phys. B* 2009, *85*, 131−138.

(40) Kau, L. S.; Hodgson, K. O.; Solomon, E. I. X-ray absorption edge and EXAFS study of the copper sites in zinc oxide methanol synthesis catalysts. *J. Am. Chem. Soc.* 1989, *111*, 7103−7109.

(41) Turnes Palomino, G.; Fisicaro, P.; Bordiga, S.; Zecchina, A.; Giamello, E.; Lamberti, C. Oxidation states of copper ions in ZSM-5 zeolites. A multitechnique investigation. *J. Phys. Chem. B* 2000, *104*, 4064−4073.

(42) Getsoian, A. G. B.; Hu, B.; Miller, J. T.; Hock, A. S. Silica-Supported, Single-Site Sc and Y Alkyls for Catalytic Hydrogenation of Propylene. *Organometallics* 2017, *36*, 3677−3685.

(43) Turnes Palomino, G.; José Cuart Pascual, J.; Rodríguez Delgado, M.; Bernardo Parra, J.; Otero Areán, C. FT-IR studies on the acidity of gallium-substituted mesoporous MCM-41 silica. *Mater. Chem. Phys.* 2004, *85*, 145−150.

(44) Connell, G.; Dumesic, J. The generation of Brønsted and Lewis acid sites on the surface of silica by addition of dopant cations. *J. Catal.* 1987, *105*, 285−298.

(45) Orazov, M.; Davis, M. E. Catalysis by framework zinc in silica-based molecular sieves. *Chemistry* 2016, *7*, 2264−2274.

(46) Parry, E. An infrared study of pyridine adsorbed on acidic solids. Characterization of surface acidity. *J. Catal.* 1963, *2*, 371−379.

(47) Ravi, M.; Sushkevich, V. L.; van Bokhoven, J. A. Towards a better understanding of Lewis acidic aluminium in zeolites. *Nat. Mater.* 2020, *19*, 1047−1056.

(48) Cordon, M. J.; Zhang, J.; Purdy, S. C.; Wegener, E. C.; Unocic, K. A.; Allard, L. F.; Zhou, M.; Assary, R. S.; Miller, J. T.; Krause, T. R.; Lin, F.; Wang, H.; Kropf, A. J.; Yang, C.; Liu, D.; Li, Z. Selective Butene Formation in Direct Ethanol-to-C_{3+}-Olefin Valorization over Zn-Y/Beta and Single-Atom Alloy Composite Catalysts Using In Situ-Generated Hydrogen. *ACS Catal.* 2021, *11*, 7193−7209.

(49) Xia, W.; Chen, K.; Takahashi, A.; Li, X.; Mu, X.; Han, C.; Liu, L.; Nakamura, I.; Fujitani, T. Effects of particle size on catalytic conversion of ethanol to propylene over H-ZSM-5 catalysts-Smaller is better. *Catal. Commun.* 2016, *73*, 27−33.

(50) Hayashi, F.; Iwamoto, M. Yttrium-modified ceria as a highly durable catalyst for the selective conversion of ethanol to propene and ethene. *ACS Catal.* 2013, *3*, 14−17.

(51) Moteki, T.; Flaherty, D. W. Mechanistic insight to C−C bond formation and predictive models for cascade reactions among alcohols on Ca- and Sr-hydroxyapatites. *ACS Catal.* 2016, *6*, 4170−4183.

(52) Yan, T.; Dai, W.; Wu, G.; Lang, S.; Hunger, M.; Guan, N.; Li, L. Mechanistic insights into one-step catalytic conversion of ethanol to butadiene over bifunctional Zn−Y/Beta zeolite. *ACS Catal.* 2018, *8*, 2760−2773.

(53) Bermejo-Deval, R.; Orazov, M.; Gounder, R.; Hwang, S.-J.; Davis, M. E. Active sites in Sn-Beta for glucose isomerization to fructose and epimerization to mannose. *ACS Catal.* 2014, *4*, 2288−2297.

(54) Sushkevich, V. L.; Vimont, A.; Travert, A.; Ivanova, I. I. Spectroscopic evidence for open and closed Lewis acid sites in ZrBEA zeolites. *J. Phys. Chem. C* 2015, *119*, 17633−17639.

(55) Cordon, M. J.; Harris, J. W.; Vega-Vila, J. C.; Bates, J. S.; Kaur, S.; Gupta, M.; Witzke, M. E.; Wegener, E. C.; Miller, J. T.; Flaherty, D. W.; Hibbitts, D. D.; Gounder, R. Dominant role of entropy in stabilizing sugar isomerization transition states within hydrophobic zeolite pores. *J. Am. Chem. Soc.* 2018, *140*, 14244−14266.

(56) Harris, J. W.; Cordon, M. J.; Di Iorio, J. R.; Vega-Vila, J. C.; Ribeiro, F. H.; Gounder, R. Titration and quantification of open and closed Lewis acid sites in Sn-Beta zeolites that catalyze glucose isomerization. *J. Catal.* 2016, *335*, 141−154.

(57) Thompson, A. R.; Oldfield, E. Solid-state scandium-45, yttrium-89, and lanthanum-139 nuclear magnetic resonance spectroscopy. *J. Chem. Soc., Chem. Commun.* 1987, *1*, 27−29.